An Effective Power Improving Method of Magnetic Field Energy Harvesters Using a Series-Connected Capacitor for Wireless Sensors in Smart Grids

Yong Li, *Senior Member, IEEE*, Na Duan, Zhaowei Liu, Xianglin Wen, Peng Li, Zhiming Wang, Jiefeng Hu, *Senior Member, IEEE*, and Zhengyou He, *Senior Member, IEEE*

***Abstract*—The low power density of a magnetic field energy harvester (MFEH) limits its applicability. Conventional methods for improving power harvesting, e.g., increasing the volume of the magnetic core, cannot effectively increase the output power density of the MFEH and it increases the burden on the transmission lines. An in-depth investigation reveals that by adding an optimal series-connected capacitor before the rectifier, the output power of the MFEH can be maximized. By reducing the net voltage applied to the magnetizing inductance, the flux accumulation is slower, lengthening the energy harvesting time, and the output power is increased. Furthermore, the output power can be maximized with an optimal series-connected capacitor. The design method of the optimal series-connected capacitor is theoretically analyzed in this article, which is only related to the load characteristics. In addition, the proposed method has a simple structure and can effectively improve the system power density of the MFEH. An experimental prototype is constructed to verify the effectiveness of the proposed method, and the results agree well with the theoretical analysis. Compared with the conventional MFEH without a series-connected capacitor, the method presented in this article can increase the harvested power by approximately 50%.**

***Index Terms*—Magnetic field energy harvester (MFEH), power density, series-connected capacitor.**

I. INTRODUCTION

In order to ensure the safe and rapid development of smart grids (SGs), wireless sensor nodes (WSNs) are widely used to monitor the real-time operating information of power lines such as voltage, current, and temperature [1]. The main bottleneck for real-time monitoring applications is the lack of self-sufficient energy. In this regard, energy harvesting (EH) technologies are promising solutions to ensure the continuous self-powering of WSNs [2]. Many energy sources in the ambient environment can be used, e.g., solar [3], [4], wind [5], vibration [6], [7], electric field [8], and magnetic field [9], [10], [11], [12], [13], [14], [15], [16].

To date, researchers have extensive research and practical experience in solar and wind power supply. These two EH technologies can effectively power the monitoring equipment. However, their output power depends on weather conditions, and the EH devices are usually large in size. The electric field energy harvester (EFEH) utilizes the potential difference in an electric field for EH, and the EFEH system often uses the ratio of the capacitive voltage divider to induce a voltage with a simple circuit and low cost. However, strict overvoltage protection and electromagnetic compatibility design are needed, which ensure electrical isolation from the front-end energy acquisition circuit to avoid damage to the electric field EH system.

According to the data from the U.K. National Grid, a typical substation generates an average magnetic field of 32 A/m, and it provides good application conditions for MFEHs [9]. Nowadays, there are two types of MFEH: cable-clamped energy harvesters and free-standing energy harvesters [10]. The free-standing energy harvester boasts advantages of easy installation and low susceptibility to core saturation. However, the power density of the free-standing energy harvester is relatively low. The cable-clamped energy harvester is similar to a current transformer, which is clapped in the transmission line. Compared to the free-standing energy harvester, it has a higher power density. Therefore, the cable-clamped energy harvester has received widespread attention in the field of SG. In this article, the MFEH analyzed is the cable-clamped energy harvester. However, with the rapid development of SGs, an increasing number of intelligent sensing developments, such as climbing robots and visual cameras are being used in the SGs. The required power of such equipment is also increasing. Therefore, improving the output power density of the MFEH as much as possible has become an urgent mission.

To improve the power density of the MFEH, many efforts have been made [11], [12], [13], [14], [15], [16], [17]. The

---

Manuscript received 18 March 2024; accepted 8 April 2024. Date of publication 12 April 2024; date of current version 16 May 2024. This work was supported in part by the Natural Science Foundation of Sichuan Province under Grant 24NSFJQ0199, in part by the Cutting-Edge Science and Technology Cultivation Project of Southwest Jiaotong University under Grant 2682022KJ005, and in part by the Fundamental Research Funds for the Central Universities under Grant 2682023ZTPV026. Recommended for publication by Associate Editor S. Panda. *(Corresponding author: Yong Li.)*

Yong Li, Na Duan, Zhaowei Liu, Xianglin Wen, and Zhengyou He are with the School of Electrical Engineering, Southwest Jiaotong University, Chengdu 610031, China (e-mail: yong_li@swjtu.edu.cn; dn2020210696@my.swjtu.edu.cn; liuzw@my.swjtu.edu.cn; m18188331008@my.swjtu.edu.cn; hezy@swjtu.edu.cn).

Jiefeng Hu is with the Institute of Innovation, Science and Sustainability, Federation University Australia, Mount Helen, VIC 3353, Australia, and also with the Centre for New Energy Transition Research, Federation University Australia, Mount Helen, VIC 3353, Australia (e-mail: hu@federation.edu.au).

Peng Li and Zhiming Wang are with the Technology Research and Development Center, Digital Grid Research Institute, China Southern Power Grid, Guangzhou 510700, China (e-mail: lipeng@csg.cn; wangzm@csg.cn).

Color versions of one or more figures in this article are available at https://doi.org/10.1109/TPEL.2024.3387688.

Digital Object Identifier 10.1109/TPEL.2024.3387688

composite core structures and optimization topologies are used to suppress the dead zone problem under a wide range of power line currents [11], which improves the output power at larger currents. However, studies show that dual cores bulge the system and increase the volume and price of the system. Liu et al. [12] considered the phase difference caused by the magnetizing inductance and established an excitation current model to accurately describe the operational characteristics of the MFEH. Then, the parameters of the magnetic core to achieve the maximum output power density of MFEHs are optimally designed. However, the designed method can only achieve the maximum output power under a single EH condition. When the EH parameters change, e.g., the primary side current, or load resistor. The original optimal design parameters of the magnetic core will not be able to achieve the maximum output power under other EH conditions. In [13], a power conditioning circuit with comprehensive control is used to achieve impedance matching to maximize the output power. This method does not consider the output characteristics of the MFEH when the core is saturated. However, saturation usually occurs in the MFEH [12]. Lu et al. [14] proposed an EH method based on impedance matching. Lu et al. [14] generates parallel resonance by matching the secondary winding of the open gap magnetic core with its excitation impedance. However, the method only considers the case where the core works on unsaturated phases. When the core is in the saturation regime, the resonance model is no longer applicable and the magnetizing inductance is a variable instead of a constant. Liu et al. [15] proposed a method to improve the performance of MFEH. The series capacitor and two switches are used to store energy and modulate the core saturation. However, the method only considers the influence of different switching states on the maximum output power, but the influence of different series capacitors on the output power has not been theoretically analyzed. The different series-connected capacitances will affect the improvement effect of the output power [16]. Moreover, the reason for the series-connected capacitor design method in the experiment has not been analyzed in [16]. Zhuang et al. [17] added an artificial magnetic field to alleviate saturation conditions and lengthen the harvesting time. However, this method is complex with the increased size and weight of the MFEH. Besides, the nonlinear variation of the MFEH internal impedance due to saturation characteristics makes it difficult to select the compensation capacitor for impedance matching.

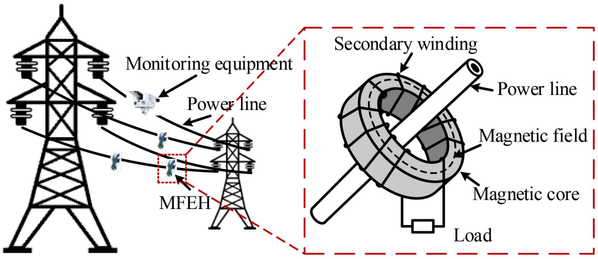

Fig. 1. Fundamental concept and structure of the MFEH installed on an AC power line.

To fill the above research gap, this article proposes an effective power improving method of magnetic field energy harvesters (MFEHs) using a series-connected capacitor. The conventional method of using a capacitor always involves resonating with the inductive impedance [18]. Thus, the current flow to the load is increased, and the power transferred to the load is increased. However, the MFEH will be saturated when high voltage is developed on the secondary winding, and the MFEH can harvest more energy when it is soft-saturated [20]. It is noted that when the MFEH is in the saturation regime, the magnetizing inductance is a variable instead of a constant [19], [22], [23]. The working condition of the capacitor that plays a resonant role is limited [18] (only when the MFEH absolutely works in the unsaturated phase). This article studies the output power characteristics when the magnetic core is in the saturation regime. Therefore, the series-connected capacitor in this article does not play the role of resonance, but the role of compensation for the adjustment of the secondary side voltage. By reducing the net voltage applied to the magnetizing inductance, the flux accumulation is slower, lengthening the EH time, and the output power is increased. Through the analysis in this article, different series-connected capacitors will affect the output power improvement effect of the MFEH system. There is an optimal series-connected capacitor that can achieve the maximum improvement of the output power. In summary, the main novelties of this article include the following.

1) Revealing the root cause of power harvesting improvement with a front-end capacitor, which is different from the conventional resonant compensation mechanism.
2) The principle of increasing output power by a series-connected capacitor in the MFEH is analyzed, which manipulates the core voltage to alleviate the saturation degree of the system, i.e., lengthen the EH time.
3) Founding the design method of the optimal capacitance, which is only related to the load resistor. The method is applicable in the case of power line current fluctuations. The theoretical design method of the optimal capacitor is given, which facilitates the practical application and design.
4) Compared to the methods discussed above, the proposed method in this article only added a series capacitor, which has a simple structure without complicated circuits or electronics, e.g., microcontrollers, switches, and MOSFETs.

II. THEORETICAL ANALYSIS

The MFEH is widely used to capture electrical energy from power lines and then supply power for sensing loads in power grids. The working scenario is shown in Fig. 1. It depicts the structure of the MFEH: the magnetic core claps on the transmission line, and the N-turn coil is wound on the magnetic core. If the primary side current is a sinusoidal current with a frequency of $\omega/2\pi$, the primary side current can be expressed as follows:

$$i_{\mathrm{p}}(t) = \sqrt{2} I_{\mathrm{p}} \sin(\omega t) \tag{1}$$

where I_{p} is the root mean square (RMS) of i_{p}, and ω is the angular frequency.

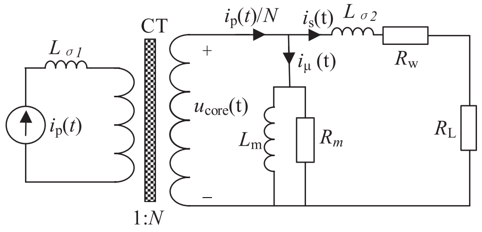

Fig. 2. Equivalent circuit of the MFEH.

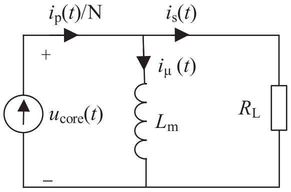

Fig. 3. Simplified circuit of the MFEH.

The equivalent circuit of the MFEH is illustrated in Fig. 2. $L_{\sigma 1}$ is the primary side leakage inductance, R_m is the magnetizing resistance, and L_m is the magnetizing inductance. R_w denotes the secondary side winding resistance; $L_{\sigma 2}$ denotes the secondary side leakage inductance; i_s(t) is the secondary side current; i_μ(t) is the magnetizing current; u_{core}(t) is the voltage across the magnetic core; and R_L is the resistance of the load.

As detailed in [16], the hysteresis loss (several mW) of the MFEH is much smaller than the output power (hundreds of mW). Thus, hysteresis loss can be ignored, and R_m can be ignored. The wire resistance is at most several ohms, which is negligible compared to the load resistance. To facilitate the analysis, this article ignores the winding resistance, i.e., $R_w = 0$. Since the permeability of the magnetic core is very high, $L_{\sigma 1}$ and $L_{\sigma 2}$ can be negligible compared with L_m. Therefore, the simplified circuit is illustrated in Fig. 3.

A. Analysis of Core Saturation

$u_{\text{core}}(t)$ is defined as the voltage across the magnetizing inductance, which can be expressed as

$$u_{\text{core}}(t) = L_m \frac{di_\mu(t)}{dt}. \tag{2}$$

The magnetizing inductance L_m can represent the saturation characteristic of the MFEH, which is obtained as [19]

$$L_m = \frac{\mu_r N^2 A}{l} = \frac{dB}{dH}\frac{N^2 A}{l} \tag{3}$$

where μ_r is the permeability of the core, A is the cross-sectional area of the magnetic core, and l is the magnetizing length of the magnetic core.

The *B*–*H* curve of the core is shown in Fig. 4. In the unsaturated phase, the *B*–*H* curve works in a relatively linear region. At this time, the magnetizing inductance is approximately regarded as a large fixed value, and the MFEH harvests energy steadily. However, in the saturated phase, the flux density B of the magnetic core reaches the maximum, and the voltage across the secondary rapidly drops to zero since the voltage that can be developed by the core is proportional to the time derivative of B.

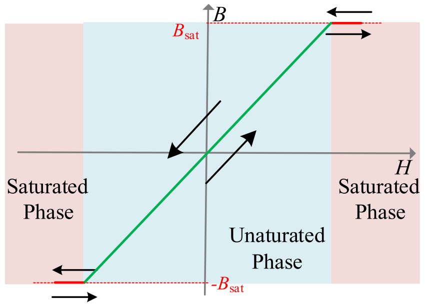

Fig. 4. *B*–*H* characteristic of a magnetic core.

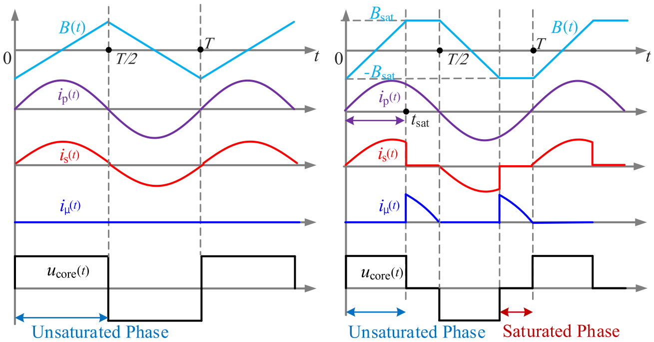

(a) (b)

Fig. 5. Two possible working states of the MFEH system. (a) MFEH is in the non-saturation regime. (b) MFEH is in the saturation regime.

Two possible working states of the MFEH system are established in Fig. 5. If the flux density B of the magnetic core does not reach the maximum in one EH period, as illustrated in Fig. 5(a). That is, there is no saturated phase, and the MFEH is considered in the nonsaturation regime. While B has reached B_{sat}, there is a saturated phase in one EH period. And, the MFEH is considered in the saturation regime, which is shown in Fig. 5(b).

By applying Kirchhoff's current law, the magnetizing current $i_\mu(t)$ can be expressed as follows [24]:

$$i_\mu(t) = \frac{i_p(t)}{N} - i_s(t). \tag{4}$$

Fig. 5 shows that the magnetizing current $i_\mu(t)$ is nearly zero in the unsaturated phase, and it increases suddenly in the saturated phase. Therefore, the secondary side current can be expressed as follows:

$$i_s(t) = \begin{cases} i_p(t)/N = \sqrt{2}I_p \sin(\omega t)/N \, (Unsaturated) \\ 0 \, (\text{Saturated}) \end{cases}. \tag{5}$$

In each EH period, the EH time, i.e., the magnetic flux density B stretching from one end of the *B*–*H* loop (-B_{sat}) to the other end (B_{sat}), is denoted as t_{sat}. The average current flowing to R_L

from 0 to t_{sat} can be expressed as

$$I_L = \frac{2}{T}\int_0^{t_{\text{sat}}} \frac{\sqrt{2}I_p \sin(\omega t)}{N} dt = \frac{4\sqrt{2}I_p(\sin(\omega t_{\text{sat}}/2))^2}{N\omega T}. \quad (6)$$

Then, the average voltage obtained across the load can be expressed as

$$U_L = I_L R_L = \frac{4\sqrt{2}I_p R_L(\sin(\omega t_{\text{sat}}/2))^2}{N\omega T}. \quad (7)$$

The average power transferred to the load can be expressed as

$$P_L = \frac{U_L^2}{R_L} = \frac{32{I_p}^2 R_L(\sin(\omega t_{\text{sat}}/2))^4}{(N\omega T)^2}. \quad (8)$$

Based on Faraday's law of electromagnetic induction, when the magnetic core is in the saturation regime, the maximum flux accumulation is equal to the integration of core voltage $u_{\text{core}}(t)$, which is the secondary-side voltage from 0 to t_{sat} [15]

$$2AB_{\text{sat}}N = \int_0^{t_{\text{sat}}} u_{\text{core}}(t)dt. \quad (9)$$

According to (8), during the EH period, for example, ωt_{sat} from 0 to π, $\sin(\omega t_{\text{sat}}/2)$ is a single increasing function. And it is always larger than zero. Therefore, when the primary side current, the parameters of the MFEH, and the load resistance are constant, P_L is increased with ωt_{sat}. From (9), t_{sat} is limited by the maximum saturation flux and the core voltage.

From (7) and (8), in a certain EH condition, i.e., a certain primary side current, a certain winding turn, a certain cross-sectional area of the magnetic core, and a certain load resistor, U_L and P_L increase with t_{sat}. Thus, lengthening t_{sat} can increase P_L. Equation (9) shows that reducing the net voltage applied to the magnetic core can increase t_{sat} when the MFEH works in a certain harvesting condition. Thus, reducing the net voltage of the magnetic core makes t_{sat} longer, that is, the output power of the MFEH can be increased. This lays the theoretical foundation for the proposed research work.

B. Analysis of the Compensation Role of the Series-Connected Capacitor

When the MFEH is series with a capacitor C_a, as shown in Fig. 7, the capacitance voltage under sinusoidal current is a concave wave. And $u_{\text{core}}(t) = u_{\text{Ca}}(t) + u_L(t)$, thus, the waveform of the core voltage is also a concave wave, as shown in Fig. 6. If t_1 is the EH time without C_a, $u_{\text{core1}}(t)$ is the core voltage without C_a; t_2 is the EH time with C_a, $u_{\text{core2}}(t)$ is the core voltage with C_a; due to the limitation of the magnetic flux saturation equation, the following equation can be derived:

$$2AB_{\text{sat}}N = \int_0^{t_1} u_{\text{core1}} dt = \int_0^{t_2} u_{\text{core2}} dt. \quad (10)$$

According to (10), if a suitable series-connected capacitor is selected, the EH time can be lengthened. That is, the net voltage of the core can be reduced, and the output power of the system can be increased.

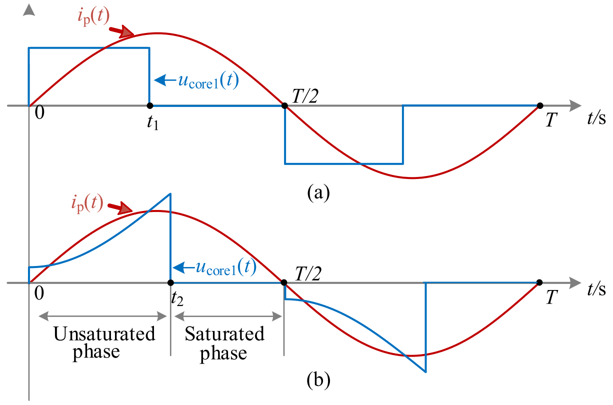

Fig. 6. Comparison of the waveforms of the MFEH. (a) Without C_a. (b) With C_a.

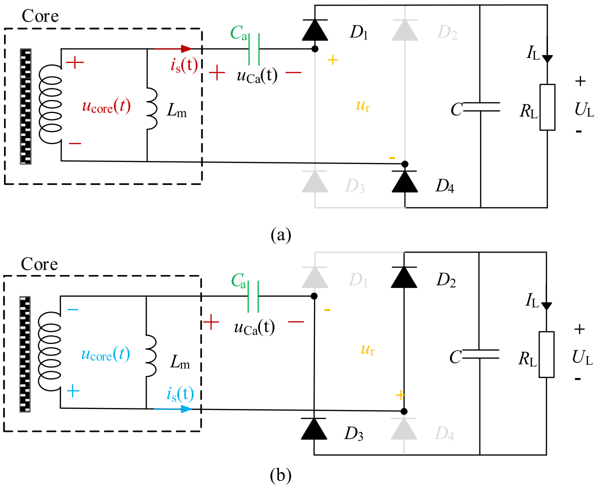

Fig. 7. Circuit example series with the capacitor C_a. (a) Before the current path reversal. (b) Time region when the current path reversal first started.

As shown in Fig. 7(a), during each EH period, the capacitor C_a is charged until the magnetic core enters the saturated phase. Once the MFEH enters the saturated phase, the magnetizing inductance instantly decreases to zero, and the core voltage becomes zero. At this instant, if $u_{\text{ca}}(t)$ is higher than U_L, the series-connected capacitor current $i_{\text{Ca}}(t)$ continually flows from C_a to the load until $u_{\text{ca}}(t)$ is equal to U_L. Subsequently, the diodes turn OFF. In contrast, if $u_{\text{ca}}(t)$ is lower than U_L, obviously current $i_{\text{Ca}}(t)$ stops with diodes being reverse biased. In this case, $u_{\text{ca}}(t)$ is maintained at a value for the rest of the present EH period. When the next EH cycle arrives, the transmission line current is reversed, and the MFEH repeats the previous process, shown as Fig. 7(b). Different series-connected capacitors will result in these two working states. The analysis of the characteristics of the output power of the MFEH with the different series-connected capacitors is illustrated in the following section.

III. OPTIMAL CAPACITOR DESIGN

When the core is not in the saturated phase, the current $i_{\text{Ca}}(t)$ flowing into C_a equals the secondary side current $i_s(t)$. If the

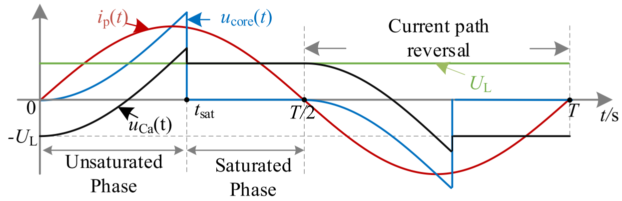

Fig. 8. Waveforms of i_p, u_{Ca}, u_{core}, and U_L when u_{Ca} (t_{sat}) $\geq U_L$.

core enters the saturated phase, L_{m} is extremely low during this period, and the current flowing into C_a equals zero. Thus, one can obtain

$$i_{C_a}(t) = \begin{cases} \sqrt{2}I_p \sin(\omega t)/N & (\text{Unsaturated}) \\ 0 & (\text{Saturated}) \end{cases}. \tag{11}$$

The relationship between the voltage and the current flowing into a capacitor can be described as

$$C_a \times \frac{du_{C_a}(t)}{dt} = i_{C_a}(t). \tag{12}$$

Substituting (11) into (12), u_{Ca} (t) when the core in the unsaturated phase can be yielded as

$$u_{C_a}(t) = \frac{\sqrt{2}I_p(1-\cos(\omega t))}{N\omega C_a} - U_0 \tag{13}$$

where U_0 is considered as a constant.

Since different capacitances will affect the magnitude of the voltage at the time point t_{sat}, there will be two possibilities, u_{Ca} (t_{sat}) $\geq U_L$ or u_{Ca} $(t_{\mathrm{sat}})$$<U_L$.

A. Analysis of U_{ca} $(t_{sat})$$\geq U_L$

If u_{Ca} (t_{sat}) $\geq U_L$, as analyzed before, the capacitor voltage u_{Ca} will decrease to U_L and remain at U_L until the beginning of the next EH period. The waveforms of $i_p(t)$, $u_{\mathrm{Ca}}(t)$, $u_{\mathrm{core}}(t)$, and U_L are depicted in Fig. 8.

According to Fig. 8, U_0 is equal to U_L, and $u_{\mathrm{Ca}}(t)$ can be expressed as

$$u_{C_a}(t) = \frac{\sqrt{2}I_p(1-\cos(\omega t))}{N\omega C_a} - U_L. \tag{14}$$

At t_{sat} instant, u_{Ca} can be obtained as

$$u_{C_a}(t_{\mathrm{sat}}) = \frac{\sqrt{2}I_p(1-\cos(\omega t_{\mathrm{sat}}))}{N\omega C_a} - U_L \geq U_L. \tag{15}$$

Substituting (7) into (15), C_a can be calculated as

$$C_a \leq T/(4R_L). \tag{16}$$

In the meanwhile, substituting (7) and (13) into (9) yields

$$2AB_{\mathrm{sat}}N = \int_0^{t_{\mathrm{sat}}} \frac{\sqrt{2}I_p(1-\cos(\omega t))}{N\omega C_a} - U_L + U_L dt$$
$$= \frac{\sqrt{2}I_p(\omega t_{\mathrm{sat}} - \sin(\omega t_{\mathrm{sat}}))}{N\omega^2 C_a}. \tag{17}$$

The waveform of C_a against t_{sat} is plotted in Fig. 9. It can be clearly seen that C_a has the same trend as t_{sat}. Consequently, under the condition of (16), only when C_a=T/(4R_L), will the power transferred to the load be maximized.

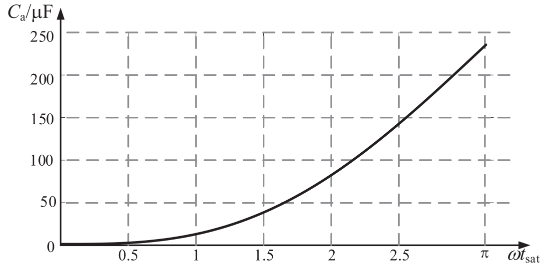

Fig. 9. Waveform of C_a against ωt_{sat} when a pomoally core in a certain condition, e.g., $I_p = 50A_{\mathrm{rms}}$, $N = 200$, and $A = 2$ cm^2.

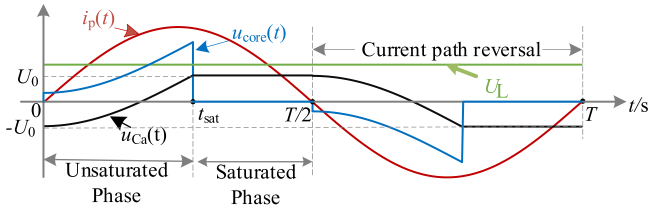

Fig. 10. Waveforms of i_p, u_{Ca}, u_{core}, and U_L when u_{Ca} (t_{sat}) $<U_L$.

B. Analysis of U_{ca} $(t_{sat})$$<U_L$

When u_{Ca} $(t_{\mathrm{sat}})$$<U_L$, the selection of the capacitor has the following restriction:

$$C_a > T/(4R_L). \tag{18}$$

Similarly, the waveforms of i_p, u_{Ca}, u_{core}, and U_L are depicted in Fig. 10. u_{Ca} (t_{sat}) can be described as

$$u_{C_a}(t_{\mathrm{sat}}) = \frac{\sqrt{2}I_p(1-\cos(\omega t_{\mathrm{sat}}))}{N\omega C_a} - U_0 = U_0 \tag{19}$$

where U_0 is a constant, and $U_0$$<U_L$.

Substituting (7) and (19) into (9), (20) can be obtained, which is shown at the bottomyes of the next page.

To facilitate the analysis, can be rewritten as

$$k = M/C_a + M_1 \tag{21}$$

where k, M, and M_1 are

$$\begin{cases} k = 2\sqrt{2}AB_{\mathrm{sat}}T(\omega N)^2/I_p \\ M = T(\omega t_{\mathrm{sat}} - 2\sin(\omega t_{\mathrm{sat}}) + \omega t_{\mathrm{sat}}\cos(\omega t_{\mathrm{sat}})) \\ M_1 = 4R_L(\omega t_{\mathrm{sat}} - \omega t_{\mathrm{sat}}\cos(\omega t_{\mathrm{sat}})) \end{cases}. \tag{22}$$

It can be seen from (22) that when the MFEH works under a certain condition, i.e., a certain magnetic core, a certain winding turns, a certain primary side current, and a certain load resistor, k will be a constant. Equation (21) only has two variables: t_{sat} and C_a. To determine the effect of t_{sat} change in an EH period on M, the first derivative and the second derivative of M against

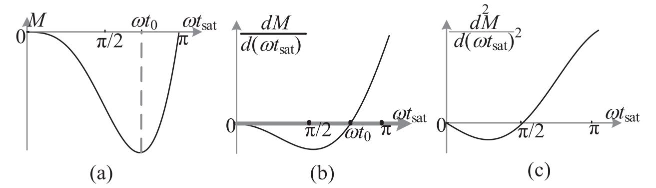

Fig. 11. Change trend of M against ωt_{sat}, the first derivative of M against ωt_{sat}, and the second derivative of M against ωt_{sat}. (a) Curve of M against ωt_{sat}. (b) First derivative of M against ωt_{sat}. (c) Second derivative of M against ωt_{sat}.

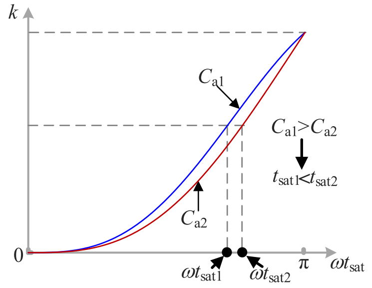

Fig. 12. Intuitive curve of k against ωt_{sat} at different C_a.

ωt_{sat} are obtained as

$$\begin{cases} M = T(\omega t_{\text{sat}} - 2\sin(\omega t_{\text{sat}}) + \omega t_{\text{sat}}\cos(\omega t_{\text{sat}})) \\ \frac{dM}{d\omega t_{\text{sat}}} = T(1 - \cos(\omega t_{\text{sat}}) - \omega t_{\text{sat}}\sin(\omega t_{\text{sat}})) \\ \frac{d^2 M}{d(\omega t_{\text{sat}})^2} = T(-\omega t_{\text{sat}}\cos(\omega t_{\text{sat}})) \end{cases}. \qquad (23)$$

According to (23), when $\omega t_{\text{sat}} = 0$ and $\pi/2$, the second derivative of M against ωt_{sat} is equal to zero. When ωt_{sat} is within the range of $(0, \pi/2)$, the second derivative of M against ωt_{sat} is less than zero. When ωt_{sat} is between $(\pi/2, \pi)$, the second derivative of M against ωt_{sat} is larger than zero. The changing trend of the second derivative of M against ωt_{sat} is plotted in Fig. 11(c). From the above analysis, it can be seen that the first derivative of M against ωt_{sat} shows a trend of first decreasing and then increasing. There are two key points, when $\omega t_{\text{sat}} = 0$, the first derivative of M against ωt_{sat} is equal to zero. And when $\omega t_{\text{sat}} = \pi$, the first derivative of M against ωt_{sat} is equal to $2T$. Therefore, the changing trend of the first derivative of M against ωt_{sat} is plotted in Fig. 11(b), and another zero crossing in Fig. 11(b) is set to ωt_0. Thus, M first decreases and then increases with increasing ωt_{sat}. Since M is equal to zero at both $\omega t_{\text{sat}} = 0$ and π, M is always less than zero in an EH period. The changing trend of M against ωt_{sat} is plotted in Fig. 11(a). Thus, under this restriction, i.e., ωt_{sat} between $(0, \pi)$, if C_{a} increases, $M/C_{\text{a}} + M_1$ will be larger for the same ωt_{sat}.

In addition, at the point of $\omega t_{\text{sat}} = 0$, $M/C_a + M_1$ is always equal to zero no matter what C_a is. And when $\omega t_{\text{sat}} = \pi$, $M/C_a + M_1$ is always equal to 2π regardless of C_a. Thus, the changing trend of $M/C_a + M_1$ against ωt_{sat} under different C_a is plotted in Fig. 12. With the same k, that is the same magnetic core, the same primary side current, and the same load resistor, a larger C_a leads to a smaller ωt_{sat}, and hence reduced power P_L transferred to the load. Consequently, under the condition of (18), only when $C_a = T/(4R_L)$, will the power transferred to the load be maximized. The design flow chart of the optimal series-connected capacitor is shown in Fig. 13.

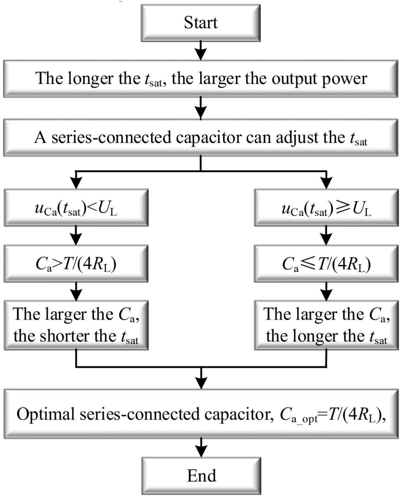

Fig. 13. Design flow chart of the optimal series-connected capacitor.

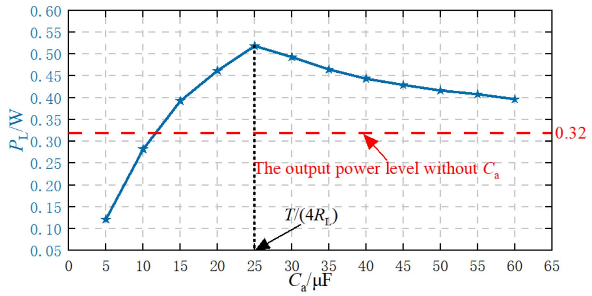

Fig. 14. P_L response with a series-connected capacitor.

According to (8), (17), and (20), the output power against C_a with an example of $I_p = 50\text{A}_{\text{rms}}$, $N = 200$, $A = 2\ \text{cm}^2$, and $R_L = 100\ \Omega$ is illustrated in Fig. 14. In this figure, when $C_a < T/(4R_L)$, the power transferred to the load increases with increasing C_a. When $C_a > T/(4R_L)$, the power transferred to the load decreases with increasing C_a. The maximized power improvement is only achieved when $C_a = T/(4R_L)$. The red line is the power level of the MFEH without C_a. If the capacitance is infinite, the capacitance path is equivalent to a short circuit, and the output

$$2AB_{\text{sat}}N = \int_0^{t_{\text{sat}}} \frac{\sqrt{2}I_p(1-\cos(\omega t))}{N\omega C_a} - U_0 + U_L dt = \sqrt{2}I_p \frac{\frac{T(\omega t_{\text{sat}} - 2\sin(\omega t_{\text{sat}}) + \omega t_{\text{sat}}\cos(\omega t_{\text{sat}}))}{C_a} + 4R_L(\omega t_{\text{sat}} - \omega t_{\text{sat}}\cos(\omega t_{\text{sat}}))}{2N\omega^2 T}. \qquad (20)$$

TABLE I
SIMULATION PARAMETERS OF THE MFEH

PARAMETERS	Value
Material	1j85
Frequency, f	50 Hz
Cross-sectional area, A	1 cm^2, 2 cm^2
Saturation magnetic induction, B_{sat}	0.6T
Series-connected capacitor, C_a	1–60 μF
Winding turn, N	200, 400
Primary side current, I_p	50 A, 100 A
Load resistor, R_L	20~500 Ω

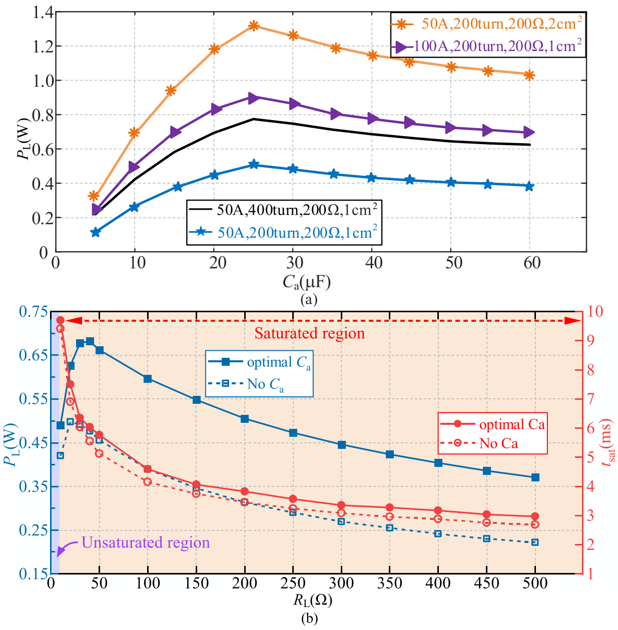

Fig. 15. Simulation results of the MFEH. (a) Waveform of the harvested power against the series-connected capacitor of the same load with $R_L = 200\,\Omega$ as reference under different EH parameters. (b) Blue: P_L-optimal C_a and P_L-without C_a. Orange: t_{sat}-optimal C_a and t_{sat}-without C_a.

power with C_a is almost the same as the output power without C_a.

IV. SIMULATION AND EXPERIMENTS

To test the proposed method, a numerical simulation is carried out. The system parameters are listed in Table I. Fig. 15(a) shows the variation curve of the harvested power transferred to the load with the series-connected capacitor under the same load and different EH parameters, e.g., I_p, A, and N. From the analysis in Section III, it is known that when $C_a<T/(4R_L)$, the power transferred to the load increases with increasing C_a. And when $C_a>T/(4R_L)$, the power transferred to the load decreases with increasing C_a. Thus, the maximized power improvement is only achieved when $C_a = T/(4R_L)$, and the optimal series-connected capacitor is only related to the load resistance. According to Fig. 15(a), it is seen that there is an optimal capacitance that enables maximum power improvement. The same load resistance always has the same optimal series-connected capacitor, no matter how other parameters vary. The simulation results in Fig. 15(a) are based on the condition that $R_L = 200\ \Omega$. The optimal series-connected capacitance is 25 μF in theoretical analysis when $R_L = 200\ \Omega$. From Fig. 15(a), the simulation results of the optimal series-connected capacitance under the same load resistor and other varied parameters are always 25 μF when $R_L = 200\ \Omega$. It agrees well with the theoretical analysis in Section III.

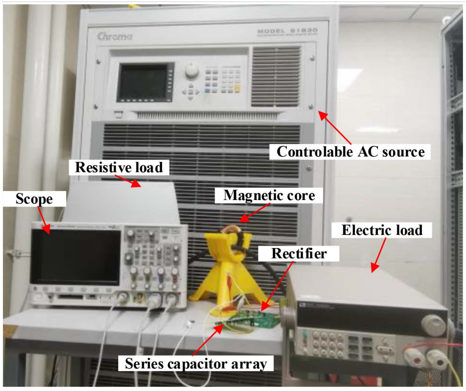

Fig. 16. Photograph of the experimental prototype.

Furthermore, Fig. 15(b) shows the simulation results of the power improvement with series-connected capacitors. The proposed MFEH achieved a power of 0.67 W under $R_L = 50\,\Omega$, $I_p = 50$ A, $N = 200$, $A = 1$ cm^2, which indicates a 52.3% increment of power compared to the harvester without using the proposed method. It is also shown that the harvesting time is lengthened from 5.2 to 5.7 ms, which verified the previous analysis in Section II.

The proposed design methodology is further verified based on an MFEH constructed in the laboratory, as shown in Fig. 16. A controllable ac source with resistive loads is used to emulate the power grid. It can generate a power frequency sinusoidal current from 0 to hundreds of amps. A permalloy magnetic core is clamped on the power line, and an array of compensation series-connected capacitors is used before the rectifier. And the experiment is verified under $I_p = 50$ A, $N = 200$, and $A = 1$ cm^2.

The typical core voltage, the capacitor voltage, and the load voltage waveforms with $R_L = 250\,\Omega$ and $R_L = 500\,\Omega$ are shown in Fig. 17(a) and (b), respectively. It can be observed that the core voltage without C_a is a square wave formed due to the existence of the rectifier circuit, as shown in the yellow waveform above Fig. 17. The core voltage with C_a is a concave wave, as shown in the yellow waveform at the bottom of Fig. 17. It is the same as the previous analysis. It is clearly seen that the EH time has been lengthened from 2.85 to 3.2 ms and from 2.4 to 2.9 ms, respectively. In addition, the output power transferred to the load increased from 0.298 to 0.39 W and from 0.212 to 0.28 W, respectively, compared to the MFEH without a series-connected capacitor. In addition, the experimental waveforms are the same as the above analysis, that is the capacitor voltage at t_{sat} is equal to the load voltage. When the secondary side of the magnetic core

TABLE II
COMPARISON BETWEEN THE METHODS

Reference	Maximum output power (mW)	I_p (A_{RMS})	A_{core} (cm^2)	B_{sat} (T)	Power density (mW/cm^2/T/A_{rms})	Additional control unit	Number of switches/coils/additional capacitors
Qian et al. [13]	5520	60	4.43	1.35	15.383	Semicontrolled active rectifier and a buck-boost control block	3/1/2
Liu et al. [15]	115.49	4	2.42	1.25	9.544	Microcontroller and an operational amplifier	2/1/1
Zhuang et al. [17]	283	10	1	1.25	22.64	Power management unit and a microcontroller	1/2/1
This article	600	50	1	0.6	20	/	0/1/1

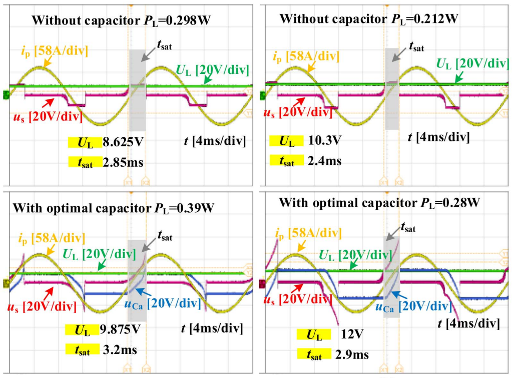

(a) (b)

Fig. 17. Experimental waveforms of typical core voltage, the capacitor voltage, and the load voltage. (a) $R_L = 250\,\Omega$. (b) $R_L = 500\,\Omega$.

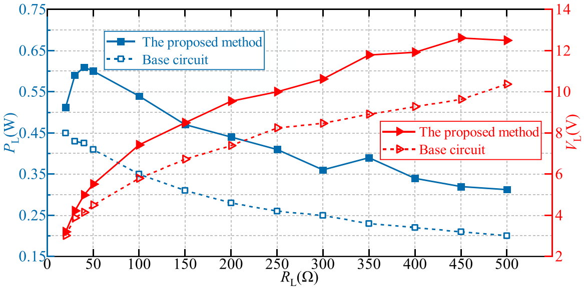

Fig. 18. Experimental results of power improvement.

is short-circuited, the capacitor voltage will remain unchanged until the next EH cycle comes.

Fig. 18 illustrates that series-connected capacitors can effectively increase the power transferred to the load compared with the basic circuit without C_a in a wide range of load resistance. The power is increased from 0.35 to 0.54 W under $R_L = 100\Omega$, which is an increase of approximately 54.3%. A 57.1% increment of power from 0.28 to 0.44 W under $R_L = 200\,\Omega$. Under the condition of $I_p = 50\,$A, $N = 200$, $A = 1$ cm^2, and $R_L = 250\,\Omega$, t_{sat} is 3.2 ms, the conduction voltage of the diode is 0.3 V, and the average power dissipation in diodes is 0.0318 W. The equivalent series resistance (ESR) of the capacitor used in the experiment is usually at the milliohm level [15]. Set it to 1 Ω with some margin, and the average power dissipated in the ESR is 1.56 mW. The load power is 0.39 W, thus, the power efficiency is 92.12%. The experiment results show that the MFEH system can achieve an ideal power boost effect by connecting an optimal capacitor in series.

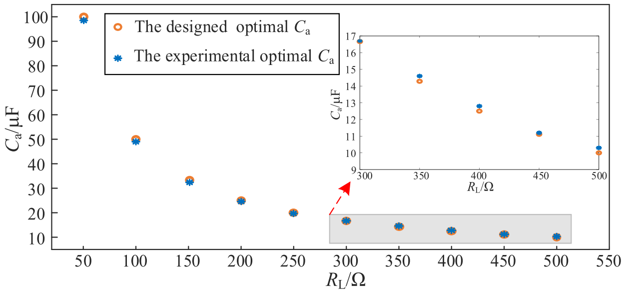

Fig. 19. Error analysis comparing designed C_a with experimental results.

The error analysis comparing designed C_a with experimental results under ten sets of R_L is shown in Fig. 19. The orange circle represents the designed optimal C_a, and the blue dots represent the experimental optimal C_a. Compared with the designed optimal C_a, the experimental optimal C_a deviation is less than 2.8%, which is high accuracy.

Table II gives the comparison results between the proposed method and the existing magnetic EH technologies. It is found that the proposed method does not increase the volume of the system, which only adds a capacitor. To increase the output power of MFEH, [13] uses a buck-boost control block, [15] and [17] use the microcontroller, which requires additional auxiliary power. Then, the volume of the system and the power loss are increased. Compared with [13], [15], and [17], only one capacitor is required to achieve the power increase of MFEH in this article, which is almost no increase in system volume and power loss. Moreover, compared with [13] and [15], higher power density can be achieved in this article. Besides, compared with [13], [15], and [17], the total number of switches, coils, and additional capacitors in this article has a minimum number, which effectively reduces the device costs. This means that the proposed method is competitive in practical application compared to existing technologies.

V. CONCLUSION

In order to improve the power density of the MFEH, a design method with a series-connected capacitor is proposed in this article. The series-connected capacitor can lengthen the EH time within every EH period, resulting in increased power harvested. An in-depth analysis further reveals that there exists an optimal capacitance. The optimal series-connected capacitor enables maximum power transfer. The design method of the optimal series-connected capacitor is presented in detail. Finally, simulation and experimental results show that, compared with conventional MFEHs, the power generated by the proposed MFEH can be improved significantly over a wide load range.

REFERENCES

[1] F. Yang, L. Du, H. Yu, and H. Peilin, “Magnetic and electric energy harvesting technologies in power grids: A review,” *Sensors*, vol. 20, no. 5, pp. 1496–1508, 2020.

[2] I. Colak, R. Bayindir, and S. Sagiroglu, “The effects of the smart grid system on the national grids,” in *Proc. Int. Conf. Smart Grid*, 2020, pp. 122–126.

[3] D. Khan et al., “A high-efficient wireless power receiver for hybrid energy-harvesting sources,” *IEEE Trans. Power Electron.*, vol. 36, no. 10, pp. 11148–11162, Oct. 2021.

[4] O. López-Lapeña, “Time-division multiplexing control of multi-input converters for low-power solar energy harvesters,” *IEEE Trans. Ind. Electron.*, vol. 65, no. 12, pp. 9668–9676, Dec. 2018.

[5] I. N. Moghaddam, B. H. Chowdhury, and S. Mohajeryami, “Predictive operation and optimal sizing of battery energy storage with high wind energy penetration,” *IEEE Trans. Ind. Electron.*, vol. 65, no. 8, pp. 6686–6695, Aug. 2018.

[6] Y. Suzuki, “Electret based vibration energy harvester for sensor network,” in *Proc. 18th Int. Conf. Solid-State Sensors, Actuators Microsyst.*, Aug. 2015, pp. 43–46.

[7] L. A. J. Friedrich, J. J. H. Paulides, and E. A. Lomonova, “Modeling and optimization of a tubular generator for vibration energy harvesting application,” *IEEE Trans. Magn.*, vol. 53, no. 11, Nov. 2017, Art. no. 8209804.

[8] P. Issouribehere, D. Esteban, F. Issouribehere, G. Barbera, and H. Mayer, “Perturbation measurements on HV overhead lines using electric field sensors,” in *Proc. IEEE Power Energy Soc. Gen. Meeting*, Nov. 2013, pp. 1–5.

[9] “National Grid substations| EMFs.info,” 2013. Accessed on: Oct. 5, 2017 [Online]. Available: http://www.emfs.info/sources/substations/substations-ng/

[10] Y. Li, Y. Yan, H. Yang, J. Hu, and Z. He, “A reconfigurable rectifier-based power improving method of free-standing two-coil magnetic field energy harvesters over a wide load range,” *IEEE Trans. Power Electron.*, vol. 38, no. 5, pp. 5638–5643, May 2023.

[11] W. Wang, C. Xu, C. Zhang, and C. Chen, “Start-up and saturation optimization of high-power energy harvester with compound topologies overhead AC transmission line,” *IEEE J. Emerg. Sel. Topics Power Electron.*, vol. 8, no. 4, pp. 3609–3617, Dec. 2020.

[12] Z. Liu, Y. Li, H. Yang, D. Na, and Z. He, “An accurate model of magnetic energy harvester in the saturated region for harvesting maximum power: Analysis, design and experimental verification,” *IEEE Trans. Ind. Electron.*, vol. 70, no. 1, pp. 276–285, Jan. 2023.

[13] Z. Qian, J. Wu, X. He, and Z. Lin, “Power maximised and anti-saturation power conditioning circuit for current transformer harvester on overhead lines,” *IET Power Electron.*, vol. 11, no. 14, pp. 2271–2278, 2018.

[14] X. Lu et al., “An on-line energy acquisition method for transmission lines based on impedance matching,” in *Proc. IOP Conf. Ser.: Mater. Sci. Eng.*, 2018, vol. 394, pp. 6867–6876.

[15] Z. Liu et al., “A novel method for magnetic energy harvesting based on capacitive energy storage and core saturation modulation,” *IEEE Trans. Ind. Electron.*, vol. 70, no. 3, pp. 2586–2595, Mar. 2023.

[16] J. Moon and S. B. Leeb, “Power electronic circuits for magnetic energy harvesters,” *IEEE Trans. Power Electron.*, vol. 31, no. 1, pp. 270–279, Jan. 2016.

[17] Y. Zhuang et al., “Improving current transformer-based energy extraction from AC power lines by manipulating magnetic field,” *IEEE Trans. Ind. Electron.*, vol. 67, no. 11, pp. 9471–9479, Nov. 2020.

[18] J. Wang and W. Chen, “Output characteristics analysis of energy harvesting current transformer,” *IEEE Sensors J.*, vol. 21, no. 20, pp. 22595–22602, Oct. 15, 2021.

[19] B. Park et al., “The magnetic energy harvester with improved power density using saturable magnetizing inductance model for maintenance applications near high voltage power line,” *IEEE Access*, vol. 9, pp. 82661–82674, Jun. 2021.

[20] J. Moon and S. B. Leeb, “Analysis model for magnetic energy harvesters,” *IEEE Trans. Power Electron.*, vol. 30, no. 8, pp. 4302–4311, Aug. 2015.

[21] Z. Liu et al., “A wide range on-line energy acquisition method for transmissionlines based on resonant choke coil,” *IET Power Electron.*, vol. 15, pp. 1047–1057, Aug. 2022.

[22] D. Seyoum, C. Grantham, and M. F. Rahman, “The dynamic characteristics of an isolated self-excited induction generator driven by a wind turbine,” *IEEE Trans. Ind. Appl.*, vol. 39, pp. 936–944, Jul./Aug. 2003.

[23] Y. Li, N. Duan, Z. Liu, J. Hu, and Z. He, “Impedance-matching-based maximum power tracking for magnetic field energy harvesters using active rectifiers,” *IEEE Trans. Ind. Electron.*, vol. 70, no. 10, pp. 10730–10739, Dec. 2022.

[24] Z. Liu, Y. Li, N. Duan, and Z. He, “An energy management method for magnetic field energy harvesters under wide-range current in railway electrification systems,” *IEEE Trans. Ind. Electron.*, vol. 71, no. 5, pp. 5360–5369, May 2024.

Yong Li (Senior Member, IEEE) received the B.Sc. and Ph.D. degrees in electrical engineering from the School of Electrical Engineering, Southwest Jiaotong University, Chengdu, China, in 2013 and 2017, respectively.

From 2017 to 2018, he was a Research Associate with the Department of Electrical Engineering, The Hong Kong Polytechnic University, where he was a Post-Doctoral Fellow. He is currently an Associate Professor with Southwest Jiaotong University, Chengdu, China. His main research interests are wireless power transfer and energy harvesting.

Na Duan received the B.Sc. degree in electrical engineering from the School of Electrical Engineering, Anhui University of Science and Technology, Huainan, China, in 2020. She is currently working toward the M.Sc. degree in electrical engineering with the School of Electrical Engineering, Southwest Jiaotong University, Chengdu, China.

Her research focuses on energy harvesting.

Zhaowei Liu received the B.Sc. degree in electrical engineering in 2020 from the School of Electrical Engineering, Southwest Jiaotong University, Chengdu, China, where he is currently working toward the Ph.D. degree in electrical engineering with the School of Electrical Engineering.

His main research interests include energy harvesting and microsensors.

Xianglin Wen received the B.Sc. degree from the School of Faculty of Information Engineering, Southwest University of Science and Technology, Mianyang, China, in 2023. He is currently working toward the M.Sc. degree with the School of Electrical Engineering, Southwest Jiaotong University, Chengdu, China.

His main research interest includes current measurement.

Peng Li received the Ph.D. degree in control engineering from the South China University of Technology, Guangzhou, China, in 2002, and the Ph.D. degree in electrical engineering from the Braunschweig University of Technology, Braunschweig, Germany, in 2004.

In 2019, he was the General Manager with Digital Grid Research Institute, China Southern Power Grid, Guangzhou, China. His research interests include stability analysis, control, optimization, dynamic simulation, data analytics for power systems and smart sensor.

Zhiming Wang received the Ph.D. degree in electrical engineering from the Department of Electronic Information Engineering, Chongqing University, Chongqing, China, in 2015.

In 2019, he was the Deputy Senior Engineer with Digital Grid Research Institute, China Southern Power Grid, Guangzhou, China. His research interests include network and communication, smart sensors, energy harvesting.

Jiefeng Hu (Senior Member, IEEE) received the Ph.D. degree in electrical engineering from University of Technology Sydney, Ultimo, NSW, Australia, in 2013.

He was an Assistant Professor with Hong Kong Polytechnic University, Hong Kong. He is currently an Associate Professor with Federation University Australia, Mount Helen, VIC¸ Australia. His research interests include power electronics, renewable energy, and smart microgrids.

Zhengyou He (Senior Member, IEEE) received the B.Sc. and M. Sc. degrees in computational mechanics from Chongqing University, Chongqing, China, in 1992 and 1995, respectively, and the Ph.D. degree in electrical engineering from Southwest Jiaotong University, Chengdu, China, in 2001.

He is currently a Professor with the School of Electrical Engineering, Southwest Jiaotong University. His research interests include signal process and information theory applied to electrical power system, and application of wavelet transforms in power systems.